

Nanoscale

Accepted Manuscript



This is an *Accepted Manuscript*, which has been through the Royal Society of Chemistry peer review process and has been accepted for publication.

Accepted Manuscripts are published online shortly after acceptance, before technical editing, formatting and proof reading. Using this free service, authors can make their results available to the community, in citable form, before we publish the edited article. We will replace this *Accepted Manuscript* with the edited and formatted *Advance Article* as soon as it is available.

You can find more information about *Accepted Manuscripts* in the [Information for Authors](#).

Please note that technical editing may introduce minor changes to the text and/or graphics, which may alter content. The journal's standard [Terms & Conditions](#) and the [Ethical guidelines](#) still apply. In no event shall the Royal Society of Chemistry be held responsible for any errors or omissions in this *Accepted Manuscript* or any consequences arising from the use of any information it contains.

PAPER

Low-Temperature CVD Synthesis of Patterned Core-shell VO₂@ZnO Nanotetrapods and Enhanced Temperature-Dependent Field-Emission Properties

Cite this: DOI: 10.1039/x0xx00000x

Received 00th January 2012,
Accepted 00th January 2012

DOI: 10.1039/x0xx00000x

www.rsc.org/

Haihong Yin,^{ab} Ke Yu,^{a*} Changqing Song,^{ab} Zhiliang Wang,^b and Ziqiang Zhu^a

VO₂ nanostructures are attractive materials because of their reversible metal–insulator transition (MIT) and wide applications in devices. When they are used as field emitters, a new type temperature-controlled field emission device may be exploited. Traditional VO₂ nanostructures synthesized via vapor transport methods are energy-guzzling, low yield, simple in morphology (quasi-1D), or by substrate clamping, that is, they are not suitable for field emission applications. To break these limitations, ZnO nanotetrapods were used as templates, and patterned core-shell VO₂@ZnO nanotetrapods were successfully grown on an ITO/glass substrate via a low-temperature CVD synthesis. SEM, TEM, EDX, XPS analyses and X-ray diffraction revealed cores and shells of these nanotetrapods were single crystal wurtzite-type ZnO and polycrystalline VO₂, respectively. These VO₂@ZnO nanotetrapods show strongly MIT-related FE properties, the emission current density at low temperature is significantly enhanced in comparison with pure VO₂ nanostructures, and about a 20 times increasing of the emission current density was observed with the ambient temperature increasing from 25 °C to 105 °C at a fixed field of 5V/μm. Although the VO₂@ZnO nanotetrapods show a worse FE performance at low temperature in comparison with pure ZnO nanotetrapods, remarkably improved FE performance was observed in high temperature range, which should be attributed to the MIT-related band bending near the interface and the abrupt resistance change across the MIT.

Introduction

VO₂ nanostructures have recently received significant attention due to their reversible Mott metal–insulator transition (MIT) at 68 °C and wide applications in devices. The MIT is characterized by a structural-electronic phase transformation from high-temperature metallic tetragonal phase (P42/mnm, R phase) to low-temperature insulating monoclinic phase (P21/c, M₁ phase),¹ which corresponds to V⁴⁺ cations along the rutile c axis, forming homopolar bonds, and undergoing a structural twist. Across the MIT, VO₂ exhibits a drastic change in optical transparency, several orders of magnitude drop in resistivity, and a small volumetric change of 0.044%.^{2–5} These unique characteristics make VO₂ promising material for applications in ultrafast optical switches,^{6, 7} electronic and gas-sensing devices,^{8–11} and electromechanical actuators.^{3, 12} Similar to other semiconductor nanostructures, the use of VO₂ nanostructures in these device applications requires precise control over their structure, spatial position, and surface density. Vapor transport technique and chemical solution synthesis are two main methods commonly adopted to prepare VO₂ nanostructures.

Using vapor transport technique, VO₂ nanostructures can be grown directly on substrates,^{13–16} which is beneficial to control the properties and integration of the nanostructures for technological applications. However, unlike other metal oxide nanostructures,¹⁷ the VO₂ nanostructures growth cannot be explained by the standard vapor-liquid-solid mechanism.^{13, 18, 19} Recent in-situ monitoring of VO₂ nanobeam growth process using optical microscopy has revealed that liquid droplets of V₂O₅ and V₆O₁₃ directly participated in the VO₂ nanobeam growth.¹⁸ These droplets were reduced to VO₂ phase and coexist with VO₂ nanobeams at the growth front. Thus, high temperature of 800–1100 °C is commonly required, quasi-1D micro/nano-structure of the products is the mostly observed morphology, and the products are commonly embedded into the substrate surface with low densities.^{13–16, 18, 19} Obviously, traditional VO₂ nanostructures synthesized via vapor transport methods are energy-guzzling, low yield, simple in morphology (1D), or by substrate clamping. Compared with VO₂, ZnO nanostructures, which comply with the standard vapor-liquid-solid growth mechanism, have abundant morphologies from 1D

to 3D, and can be easily synthesized via vapor transport methods.²⁰ Moreover, ZnO nanostructures with a wide direct band gap of 3.34 eV have been demonstrated to be a promising oxide semiconductor for many optoelectronic devices, such as UV lasers,²¹ solar cells, nanogenerators,²² UV photodiodes,^{23,24} and field emission (FE) emitters.²⁵⁻²⁸ Thus, taking ZnO nanostructures as templates and constructing ZnO-core/VO₂-shell nanostructures may be a feasible way to overcome aforementioned obstacles of VO₂ nanostructures, meanwhile, the combination of VO₂ and ZnO may lead to a new type MIT-type optoelectronic nanodevice.

Previous work in our laboratories as well as others has demonstrated that the work function of pure VO₂ shows an abrupt decrease across the MIT process.^{29,30} Thus, pure VO₂ nanostructures show strongly temperature-dependent and MIT-related FE properties. However, these VO₂ nanostructures, which were synthesized via a hydrothermal route, were not directly grown on the substrate but painted by a screen-printing method.³⁰ Thus, large contact resistances were formed between the substrate and VO₂ nanostructures. Although VO₂ nanostructures can be directly grown on the substrate using vapor transport methods, they are not suitable for FE applications because they are embedded in the substrate surface. In addition, the resistance of M₁ phase VO₂ is too large, thus their FE current density at room temperature is too low (2.01 μA/cm²) to be of any practical application.³⁰ In large quantities of literatures, ZnO nanostructures have been demonstrated to be a good cold cathode material for FE applications.²⁵⁻²⁸ By constructing ZnO-core/VO₂-shell nanostructures and growing them directly on the substrate, the contact resistance and the structure resistance can be significantly decreased, thus tuned FE properties can be reasonably expected. In this paper, taking tetrapod-like ZnO nanostructures as templates and using a vapor transport method, 3D patterned ZnO-core/VO₂-shell nanotetrapods were selective-area grown on a glass substrate at low temperature. These ZnO@VO₂ nanotetrapods show strongly temperature-dependent FE properties; the current density at low temperature is significantly enhanced in comparison with pure VO₂ nanostructures, and about a 20 times increase of the emission current was observed when the ambient temperature increased from 25 °C to 105 °C at a fixed field of 5V/μm. The controllable growth of patterned ZnO@VO₂ nanotetrapods and their MIT-related FE properties provide a feasible strategy to break through obstacles of traditional synthesized VO₂ nanostructures and explore new type of temperature-controlled field emitters.

Experimental Section

Synthesis of patterned ZnO and VO₂@ZnO nanotetrapods

The synthesis strategy for patterned VO₂@ZnO nanotetrapods is to synthesize 3D ZnO nanotetrapods and then coated with VO₂, as schematically illustrated in the inset of Fig.1. Briefly, a mixture of high purity ZnO powder (50 wt%) and graphite

powder (50 wt%) was inserted into the centre of the fused-quartz tube mounted in a horizontal tube furnace. A stainless

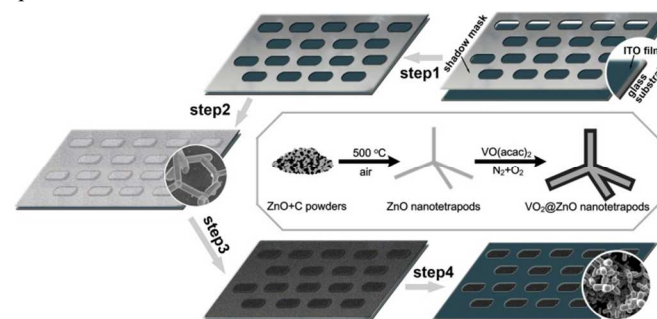


Fig. 1 Schematic of the fabrication process of patterned VO₂@ZnO nanotetrapods. Step 1: mask and substrate preparation. Step 2: thermal evaporation growth of ZnO nanotetrapods. Step 3: coating VO₂ on ZnO nanotetrapods. Step 4: removal of the mask.

mask was tightly attached to a glass substrate with a thin ITO film. The substrate/mask was placed downstream from the vapor direction for collection of the products, and a 10 cm gap was set between the source and the substrate. Then, the source temperature was raised to 500 °C at a rate of 10 °C min⁻¹ and held 50 min under a constant N₂ (purity 99.9%) flow of 400 sccm. After that, the outlet of the tube furnace was opened, immediately introducing air into the system while the N₂ flow was maintained unchanged. After the furnace was cooled to room temperature, a light white ZnO layer was found being deposited on the substrate/mask. Subsequently, the substrate/mask covered with ZnO nanotetrapods was located at the tube centre of a CVD system. Vanadyl acetylacetonate (VO(acac)₂) was taken as vanadium precursors and placed in a special evaporating chamber, where temperature was controlled at 200 °C. Before heating, the CVD system was pumped to expel oxygen in the tube, and pure nitrogen gas was introduced to reach the pressure of atmosphere. Then, the reaction chamber was heated to 510 °C. A mixture of nitrogen (92%) and oxygen (8%) at a constant flow rate of 50 sccm was used to carry the precursor vapor to the reaction chamber. The reaction lasted for 30 min, and then the system was cooled down to room temperature under an N₂ flow, the color of the product changed from light white to gray. After removal of the mask, patterned VO₂@ZnO nanotetrapods were obtained on the glass/ITO substrate. The whole synthesis process is shown in Fig. 1. For comparison, another sample of patterned ZnO nanotetrapods was also synthesized on the glass/ITO substrate using the same method.

Characterization The morphologies and size of the product were characterized by field-emission scanning electron microscopy (FESEM, JEOL-JSM-6700F) and transmission electron microscopy (JEOL, JEM-2100). The crystal structure was characterized by X-ray diffraction (XRD, Bruker D8 Advance diffractometer) using monochromatized Cu K α radiation ($\lambda = 1.5418\text{\AA}$). Differential scanning calorimetry (DSC DSC-60, SHIMADZU) experiment was performed in nitrogen flow in the range from 25 to 97 °C with a heating rate of 1 °C/min.

Field-Emission Measurement For field-emission investigation, the ITO/glass substrate with patterned $\text{VO}_2@ZnO$ nanotetrapods (as a cathode) was separated from a phosphor/ITO/glass anode by two Teflon spacers with a thickness of 400 μm . FE properties were measured with a high vacuum level of about 5×10^{-5} Pa at different temperatures using transparent anode imaging technique. The measured area was $1 \times 1 \text{ cm}^2$, and the actual emission area covered by nanomaterial was calculated to be 15 mm^2 . In the measurement, the turn-on field is determined as the field needed to produce a current density of 10 $\mu\text{A}/\text{cm}^2$, and the threshold field is the field needed to produce a current density of 1 mA/cm^2 .

Results and discussion

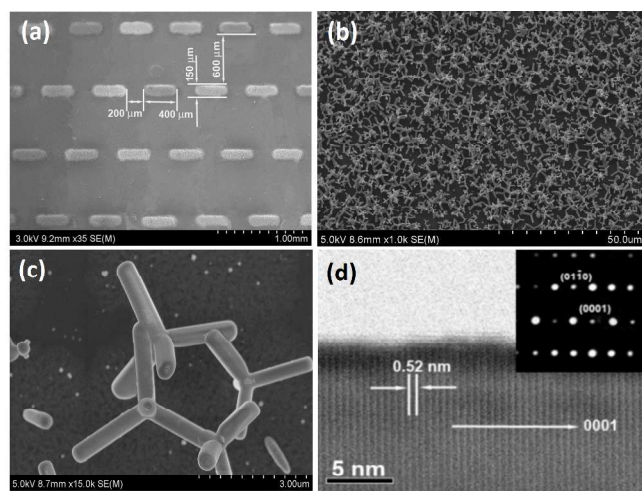


Fig. 2 (a) Low-, (b) medium-, and (c) high-magnification SEM images of ZnO nanotetrapods synthesized by a thermal evaporation method. (d) High-resolution TEM image of a single nanorod of a tetrapod ZnO. Upper inset in (d) is the corresponding SAED pattern.

Under the restriction of the mask, patterned ZnO nanotetrapods were successfully grown on a glass substrate at 500 °C using a thermal evaporation method. The representative SEM images of the products are shown in Fig. 2a–c. In Fig. 2a, each deposited unit takes an oblong shape. The dimension of each unit is about 400 μm in length and about 150 μm in width, and the distance between the two neighbouring units is about 200 μm in row and about 600 μm in column (see Fig. 2a), agreeing well with the pattern of the mask. The nanostructures inside the block show uniform tetrapod-like ZnO nanorods with good quality and high yield (Fig. 2b). The diameters of four legs were about 600 nm, and their lengths were in the range 2–5 μm (Fig. 2c). High-resolution (HR) TEM image for a single leg (Fig. 2d) exhibits clear lattice fringes, indicating a single crystal. The corresponding SAED pattern (the inset of Fig. 2d) indicates that legs of as-prepared ZnO nanotetrapods grew along the [0001] direction. The spacing between two adjacent lattice planes is close to 0.52 nm and consistent with the (0001) planes of wurtzite ZnO. In traditional synthesis of VO_2 nanostructures using a vapor transport method, V_2O_5 or VO_2 powder are the commonly used source. Thus, high temperature of 800–1100 °C is commonly required, and most of the products are embedded

into the substrate surface. Utilizing the low sublimation and pyrolysis temperature of the precursor ($\text{VO}(\text{acac})_2$), VO_2 films are successfully deposited on the surface of ZnO nanotetrapods

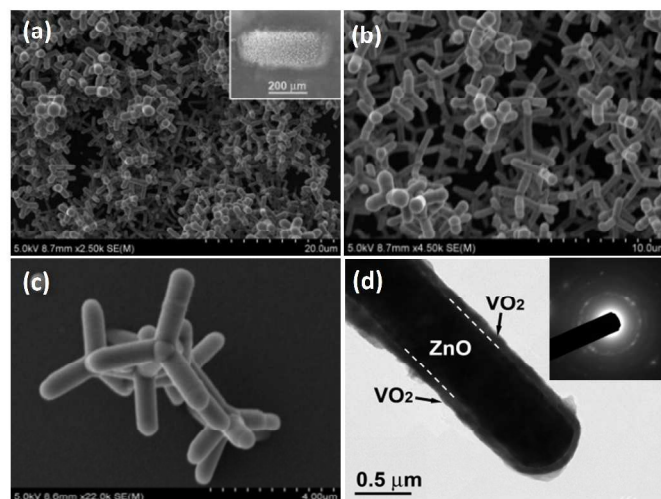


Fig. 3 (a) Low-, (b) medium-, and (c) high-magnification SEM images of $\text{VO}_2@ZnO$ nanotetrapods synthesized by a thermal evaporation method. (d) High-resolution TEM image of a single nanorod of a tetrapod $\text{VO}_2@ZnO$. Upper inset in (d) is the corresponding SAED pattern.

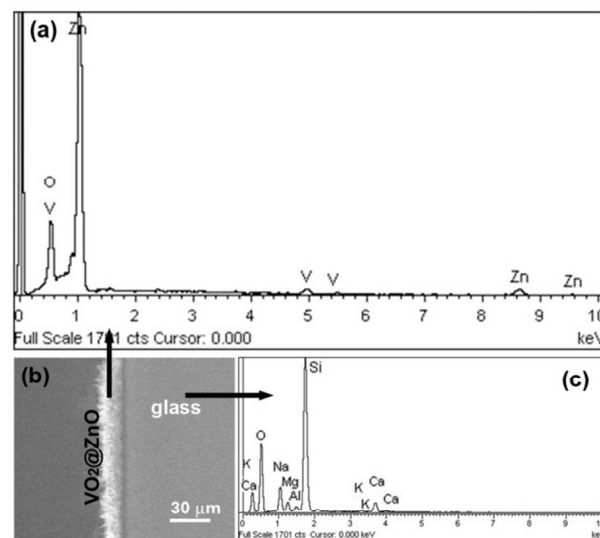


Fig. 4 (a) EDX spectra of $\text{VO}_2@ZnO$ nanotetrapods. The semi-quantitative elemental analysis result is listed in the EDX panel. (b) The side view of $\text{VO}_2@ZnO$ nanotetrapods on the glass substrate. (c) EDX spectra of the glass substrate.

at a relative low temperature of 510 °C, forming 3D VO_2 -shell@ZnO-core nanostructures. As shown in Fig. 3a–c, most of the products still retained initial tetrapod structure, and rough surface can be clearly observed, showing a film coating on ZnO nanotetrapods. The corresponding TEM image for a single leg (Fig. 3d) indicates that the diameter of the legs increased remarkably and a thin VO_2 film about 90 nm thick was coated on the ZnO core. In the SAED patterns (the inset of Fig. 3d), the regular polycrystalline diffraction rings shows that the shell is a polycrystalline VO_2 film. The EDX spectra from the sample (Fig. 4a) indicate the presence of element V besides elements Zn and O, confirming the components of VO_2 and

ZnO. In addition, the glass substrate can be verified by the detection of K, Ca, Na, Mg, Al, Si and O elements in the EDX spectra (Fig. 4b).

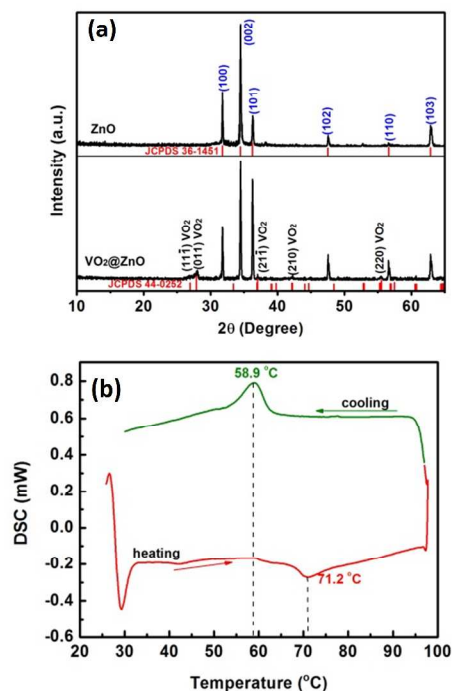


Fig. 5 (a) XRD patterns of obtained ZnO and VO₂@ ZnO nanotetrapods. (b) DSC thermal spectra of as-obtained VO₂@ZnO nanotetrapods showing a narrow heating cooling hysteresis and excellent MIT behavior.

Among many polymorphs of VO₂, only rutile-type VO₂(M₁/R) undergoes a first-order reversible metal-insulator transition between M₁ phase and R phase. For phase confirmation of the shell coating, XRD analyses were utilized. The XRD pattern of pure ZnO nanotetrapods (Fig. 5) shows only peaks of wurtzite ZnO (JCPDS 36-1451) with lattice constants of $a = 11.516 \text{ \AA}$, $b = 3.566 \text{ \AA}$, $c = 4.373 \text{ \AA}$. No peaks of any other impurities were detected in the spectra, revealing the high phase purity of ZnO nanotetrapods. For VO₂@ZnO nanotetrapods, the XRD measurement verified that there was a new phase in addition to wurtzite ZnO as shown in Fig. 5, which could be indexed to M₁ phase VO₂ (JCPDS 44-0252). No characteristic peak of other phases or impurities, such as V₂O₅, ZnV₂O₆ or Zn₂V₂O₇, was observed, confirming the components of the VO₂ and ZnO in the core-shell nanotetrapods. The first-order phase transition of VO₂@ ZnO nanotetrapods was investigated by monitoring the enthalpy change using DSC analysis. As shown in Fig. 5b, VO₂@ ZnO nanotetrapods show a heating cooling hysteresis and an excellent MIT behaviour at 71.2 °C. It should be noted that the transition temperature in the present study is higher than 68 °C, which is the value reported in the literature for undoped VO₂ films or VO₂ bulk single crystals. Similar phenomena have been observed in either VO₂-based bilayer films (VO₂/ZnO, VO₂/TiO₂, and VO₂/Al₂O₃) or VO₂-based core-shell nanostructures (VO₂@TiO₂), and can be interpreted by the effect of interfacial strain.^{4, 31-33} In VO₂@ZnO core-shell

nanostructures, the mismatched interface creates a tensile strain in the *c*-direction of VO₂ (Poisson's effect). The tensile strain in *c*-direction causes an increased V⁴⁺-V⁴⁺ distance and would

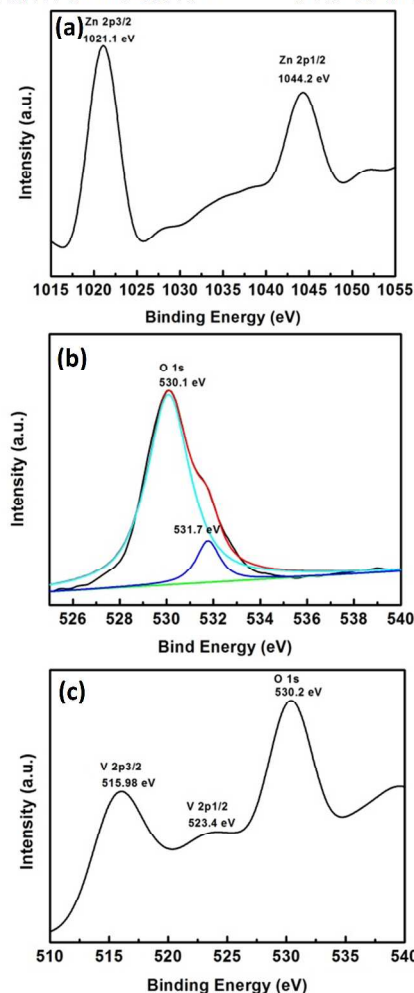


Fig. 6 XPS spectra of the as-prepared ZnO and VO₂@ ZnO nanotetrapods: (a) and (b) High resolution spectra for Zn 2p and O 1s, respectively; (c) High resolution spectra for V 2p and O 1s.

raise the activation barrier for direct overlapping of *d*-orbitals. This increased activation barrier further stabilizes the covalent monoclinic phase and hinders the transformation to metallic rutile structure, leading to the observation of higher MIT temperatures.

To further investigate the chemical state of the as-prepared ZnO and VO₂@ZnO nanotetrapods, X-ray photoelectron spectroscopy (XPS) was carried out, and their corresponding spectra were shown in Fig. 6a-c. The binding energies obtained in the XPS analysis were corrected for specimen charging by referencing the C 1s to 284.8 eV. Fig. 6a and b show Zn 2p and O 1s spectra of ZnO nanotetrapods, respectively. The Zn 2p core-level spectra illustrate two representative peaks located at 1021.1 eV and 1044.2 eV, corresponding to the Zn 2p_{3/2} and Zn 2p_{1/2} of Zn²⁺, respectively. The O 1s spectrum shows mainly a peak at 530.1 eV (O²⁻) with a small shoulder at about 531.7 eV. The main peak centred at 530.1 eV is attributed to O²⁻ ions on wurtzite structure of the hexagonal Zn²⁺ ion array. The shoulder

at 531.7 eV is associated with hydroxidic, such as absorption of OH groups. Considering oxygen vacancy is the main surface defect in ZnO nanostructures, the oxygen vacancies should be

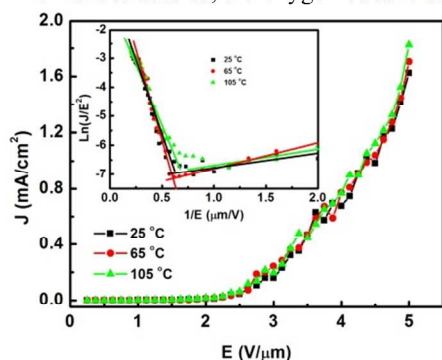


Fig.7 Dependence of the FE current density J on the applied electric field strength E of ZnO nanotetrapods for different temperatures. Inset, the corresponding Fowler-Nordheim (F-N) plots.

the main sites for hydroxidic absorption. For $\text{VO}_2@ZnO$ nanotetrapods, it is verified that both vanadium and oxygen are found existing in the samples' shell (Fig. 6c). The V 2p core level spectra illustrate two representative peaks located at 515.98 eV and 523.4 eV, corresponding to the V $2p_{3/2}$ and V $2p_{1/2}$ of V^{4+} , respectively. The O 1s peak located at 530.2 eV is also observed in Fig. 6c, corresponding to the O 1s of O^{2-} .

The influence of the ambient temperature on the pure ZnO FE properties was first investigated before the discussion of $\text{VO}_2@ZnO$ FE properties. Fig. 7 shows the relationship between the emission current density (J) and the applied electric field (E) for ZnO nanotetrapods at the temperatures of 25, 65 and 105 °C, respectively. Obviously, the three J - E curves approximately coincide with each other, and only a tiny fluctuation is observed in the three curves, revealing a

negligible influence of temperature on FE properties of pure ZnO nanotetrapods. The corresponding turn-on fields is ~ 1.75 – 2 $\text{V}/\mu\text{m}$, and the threshold electric fields is ~ 4.35 $\text{V}/\mu\text{m}$. The Fowler-Nordheim (F-N) plots are shown in the inset of Fig. 7. These straight lines indicate that the emitting electrons are mainly resulted from field emission. It is noted that these F-N plots are composed of two discrete linear sections. The first sections are placed in the fields greater than turn-on fields, having a negative slope in the F-N plot. This implies that the electron emission at high fields followed the FN theory. However, the second sections, which are placed in the low-field region, have a positive slope in F-N plots and can be attributed to the contribution of surface states.^{34, 35}

Unlike pure ZnO nanotetrapods, FE properties of $\text{VO}_2@ZnO$ nanotetrapods are strongly dependent on the ambient temperature. Fig. 8a shows typical plots of FE current density versus applied field (J - E) of $\text{VO}_2@ZnO$ nanotetrapods at different temperature (from 25 to 105 °C) in a whole heating/cooling process. It is obvious that the emission current density J increases exponentially with the applied field E , and the FE properties can be remarkably improved by increasing the temperature. In the heating process, the turn-on fields at 25, 45, 65, 85 and 105 °C decreased gradually with the ambient temperature, whose values are 3.6, 3.2, 2.7, 2.37, and 1.3 $\text{V}/\mu\text{m}$ respectively. Meanwhile, the threshold electric fields also decreased with the ambient temperature. Their values at 65, 85 and 105 °C are 4.7, 3.9 and 3.4 $\text{V}/\mu\text{m}$, respectively. The current density is also observed increasing significantly with the temperature (Fig. 8a). In our previous work, FE current density for pure VO_2 nanostructures at low temperature is too weak ($2.01 \mu\text{A}/\text{cm}^2$ at 25 °C, and $202 \mu\text{A}/\text{cm}^2$ at 64 °C) to be of any

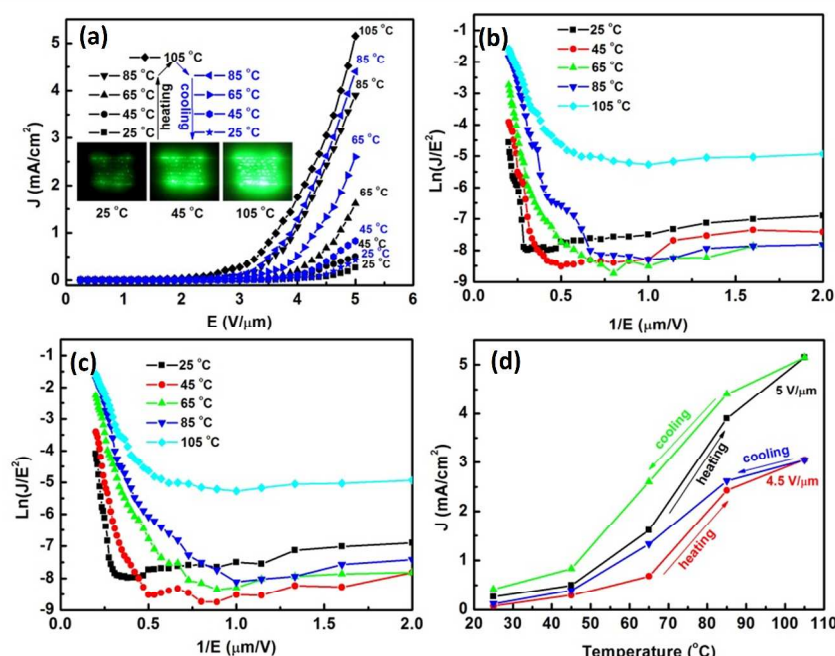


Fig.8 (a) Dependence of the FE current density J on the applied electric field strength E of $\text{VO}_2@ZnO$ nanotetrapods for different temperatures in a heating/cooling process. Insets, the electron emission images (applied field around $5 \text{ V}/\mu\text{m}$) in the heating process for 25, 65 and 105 °C, respectively. (b) FE current density J at

different temperature for fixed field E of 4.5 and 5 V/ μm , respectively. Note that the curves show a heating cooling hysteresis loop. (c) and (d) The Fowler-Nordheim (F-N) plots corresponding to the heating process and the cooling process, respectively.

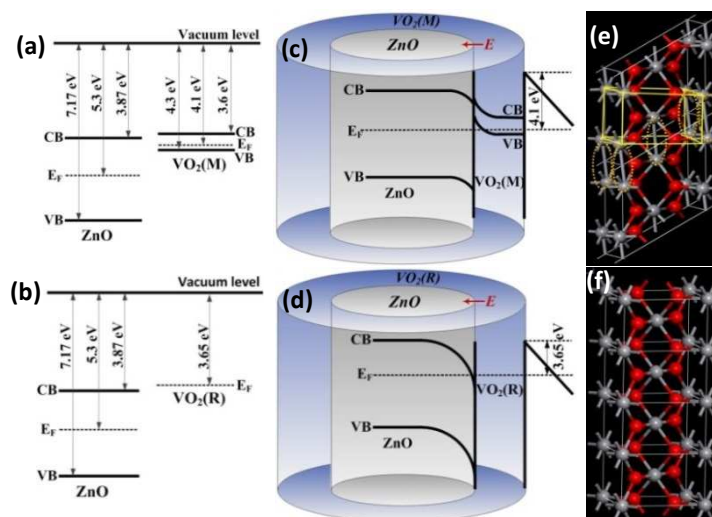


Fig.9 (a-b) Schematic diagram of the band configuration for ZnO, VO₂(M₁) and VO₂(R) crystals. (c-d) Band bending at the interface of VO₂@ZnO nanotetrapods before and after the MIT process. The vector E is the built-in electric field at the interface. (e-f) The atomic structure of VO₂ for M₁ phase (low-temperature) and R phase (high-temperature), respectively. Red spheres: O atoms, gray spheres: V atoms. Thick yellow box (solid lines) in the monoclinic structure emphasizes the similarity between the two phases. Note that the V-V bonds in the monoclinic structure (marked with dashed yellow ellipses) break after transforming to the rutile structure.

practical application.³⁰ Here, the emission current density for VO₂@ZnO nanotetrapods shows a significant elevation in all temperature range especially in the low temperature. Under the applied field of 5 V/ μm , the maximum emission current density at low temperature (25, 45 and 65 °C) are 0.26, 0.5 and 1.61 mA/cm², and the values increased to 3.9 and 5.2 mA/cm² when the temperature increased to 85 and 105 °C, respectively. The inset of Fig. 8a shows the real-time emission images of patterned VO₂@ZnO nanotetrapods at 25, 65 and 105 °C, respectively, recorded by CCD camera and tested at the applied field of 5 V/ μm . Although the emitting intensity at the room temperature (25 °C) is the lowest, there is a remarkable improvement in the emitting intensity compared to pure VO₂ nanostructures. With the temperature increasing, the emitting intensity is observed further increasing significantly. Considering the negligible influence of the temperature on pure ZnO nanotetrapods, the strongly temperature-dependent FE properties of VO₂@ZnO nanotetrapods should be attributed to the introduction of VO₂ shell.

The Fowler-Nordheim (F-N) plots for the heating and the cooling process are shown in Fig. 8b and 8c, respectively. These straight lines in high-field region indicate that the emitting electrons are mainly resulted from field emission. For temperature-dependent FE, the total current density may come from both field emission and thermionic emission, which can be analysed by the Richardson–Dushman equation.^{35, 36}

$$J = J_E + J_T \quad (1)$$

$$J = A \frac{\beta^2 E^2}{\phi} \exp\left(-\frac{B\phi^{3/2}}{\beta E}\right) \left[\frac{\theta}{\sin \theta}\right] + A_R T^2 e^{-\phi/kT} \quad (2)$$

Where J_E and J_T are the field current and thermionic current density, respectively. $A=1.54 \times 10^{-6} \text{ AeVV}^{-2}$, $B=6.83 \times 10^9 \text{ eV}^{-3/2} \text{Vm}^{-1}$, β is the field enhancement factor, and ϕ is the work function of the emitter material. $A_R=120 \text{ Acm}^{-2} \text{K}^{-2}$, T is the emitter temperature, k is the Boltzmann constant, and θ is the temperature correction factor which can be given by:

$$\theta \approx \frac{2.2\pi(kT/q)\phi^{1/2}}{1.959E} \quad (3)$$

For VO₂@ZnO nanotetrapods, the ambient temperature is not too high, therefore, the value of $[\theta/\sin\theta]$ is always equal to 1.0 and the contribution of thermionic emission is much smaller than FE current density. Thus, the temperature-dependent FE properties of VO₂@ZnO do not come from thermionic emission, but is predominated by FE emission. Moreover, it is noted that the J - E curves for the heating and the cooling process at the same temperature are not coincide with each other, as shown in Fig. 8a. The FE current density in the heating/cooling process for different temperature was recorded under two fixed fields of 4.5 and 5 V/ μm . As shown in Fig. 8d, it is clear that the curves show a heating cooling hysteresis loop, revealing the temperature-dependent FE properties strongly related to the MIT of VO₂.

Based on the above experimental results, the introduced VO₂ shell plays a vital role in the temperature-dependent FE properties. The role and influence of the introduced VO₂ shell can be analysed by the change of energy band structures. In previous studies, work functions of ZnO, VO₂(M₁) and VO₂(R) have been reported to be 5.3, 4.1 and 3.65 eV, respectively,^{28, 30} indicating that ZnO crystal has a Fermi level (E_F) lower than VO₂(M₁) and VO₂(R) (Fig. 9a and b). For VO₂@ZnO nanotetrapods, both ZnO and VO₂ have the same Fermi energy

level at the core-shell interface, thus a staggered band offset is formed near the interface. Because of the MIT properties of VO₂, the energy structure at the interface of ZnO/VO₂ is different before and after the phase transition. Their schematic diagrams are shown in Fig. 9b and c, respectively. At low temperature, it can be seen from Fig. 9c that the conduction band of ZnO is higher than that of VO₂(M₁) and a built-in electric field (the vector *E*) is formed at the interface. When VO₂(M₁)@ZnO nanotetrapods are used as the cathode, the applied field and the built-in electric field are in the same direction. The electrons in the ZnO core can easily transfer to VO₂(M₁) shell, and then tunnelling emit to the vacuum level. Because the work function of VO₂(M₁) (4.1 eV) is lower than that of ZnO (5.3 eV), a better FE performance should be obtained in VO₂@ZnO nanotetrapods at low temperature. However, the measurement indicates that pure ZnO nanotetrapods show a better FE performance than low-temperature VO₂@ZnO nanotetrapods (Fig. 7 and Fig. 8a). So the band bending at the interface cannot interpret the decreased FE performance in VO₂(M₁)@ZnO nanotetrapods. She et al. and Zhao et al. have reported that the field emission performance of emitters was strongly correlated with their resistance and the oxygen vacancy density. A ZnO emitter with low resistance and high oxygen vacancy density often had better FE performance.^{37, 38} For bare ZnO nanotetrapods, the oxygen vacancies serve as donors to supply electrons to the conduction band, showing a high conduction. For VO₂(M₁)@ZnO nanotetrapods, the coated film will heal the oxygen vacancies and decrease the vacancy concentration to some extent, leading to a lower conduction of ZnO cores. Moreover, VO₂ is a typical well-known Mott insulator. V-V covalent bonds are formed along the rutile *c* axis due to the strong local electron-electron interactions (Fig. 9e), leading to high resistance in M₁ phase. In the FE process of VO₂(M₁)@ZnO nanotetrapods, both the high resistance of VO₂(M₁)-shell and the lower conduction of ZnO cores together raise the applied field needed to be added to reach a certain current density. Thus, lower emission current density and higher turn-on and threshold fields are observed in VO₂@ZnO nanotetrapods at low temperature. In high temperature range, VO₂ shell transforms from the M₁ phase to the metallic R phase. Because the work function of VO₂ decreases from 4.1 eV (M₁ phase) to 3.65 eV (R phase), the built-in electric field (the vector *E*) at the interface of VO₂/ZnO is further enhanced, which promote electrons transferring from ZnO core to VO₂(R) shell. After the MIT happened, the V-V bonds in the M₁ phase break (Fig. 9f) and R phase rutile structure is formed (Fig. 9g), causing an abrupt decrease of structure resistance. The high conductivity of VO₂(R) is beneficial to the movement of the injected electrons to the VO₂ surface. Due to the lower work function (3.6 eV) of VO₂(R), these electrons also can easily tunnelling emit to the vacuum level. Thus, higher emission current density, lower turn-on and threshold fields are observed in FE measurement of VO₂@ZnO nanotetrapods in high temperature range, that is, a significant enhancement of FE performance was obtained.

Conclusions

In summary, ZnO nanotetrapods were used as templates, and patterned VO₂@ZnO nanotetrapods were successfully synthesized on an ITO/glass substrate via a low-temperature CVD method. These VO₂@ZnO nanotetrapods showed strongly temperature-dependent FE properties. The turn-on fields and the threshold fields decreased gradually with the temperature, and about 20 times increasing of the emission current density (at 5V/μm) was observed. At low temperature, VO₂@ZnO nanotetrapods showed a worse FE performance than bare ZnO due to the large resistance of VO₂ (M₁), whereas, a significant FE enhancement was observed in the high temperature range and can be attributed to high conductivity and low work function of VO₂(R). The synthesis of VO₂@ZnO nanotetrapods and their temperature-dependent FE properties are beneficial to exploring new type MIT-related FE devices.

Acknowledgements

The authors acknowledge financial support from the NSF of China (Grant Nos. 61204018, 61274014, 61290304, 61371111, 61371112 and 81371663), the NSF of Jiangsu Province (Grant No. BK20141239), Innovation Research Project of Shanghai Education Commission (Grant No. 13zz033), Education Committee of Jiangsu Province (Grant No. 13KJB510029), Project of Key Laboratory of Polar Materials and Devices (Grant No. KFKT2014003), and Six Top Talents of Jiangsu Province (Grant No. XCL-013).

Notes and references

^a Key Laboratory of Polar Materials and Devices (Ministry of Education of China), Department of Electronic Engineering, East China Normal University, Shanghai, 200241, P. R. China. Fax: +86-21-54345198; Tel: 13611980114; E-mail: yk5188@263.net

^b School of Electronics and Information, Nantong University, Nantong, 226019, P. R. China.

1. F. J. Morin, *Phys. Rev. Lett.*, 1959, **3**, 34.
2. J. Cao, E. Ertekin, V. Srinivasan, W. Fan, S. Huang, H. Zheng, J. W. L. Yim, D. R. Khanal, D. F. Ogletree, J. C. Grossman and J. Wu, *Nat. Nanotechnol.*, 2009, **4**, 732-737.
3. S. Lee, C. Cheng, H. Guo, K. Hippalgaonkar, K. Wang, J. Suh, K. Liu and J. Wu, *J. Am. Chem. Soc.*, 2013, **135**, 4850-4855.
4. Y. Li, S. Ji, Y. Gao, H. Luo and M. Kanehira, *Sci. Rep.*, 2013, **3**, 1370.
5. J. Wu, Q. Gu, B. S. Guiton, N. P. de Leon, O. Lian and H. Park, *Nano Lett.*, 2006, **6**, 2313-2317.
6. A. Cavalleri, C. Tôth, C. Siders, J. Squier, F. Ráksi, P. Forget and J. Kieffer, *Phys. Rev. Lett.*, 2001, **87**, 237401.
7. E. E. Chain, *Appl. Optics.*, 1991, **30**, 2782-2787.
8. E. Strelcov, Y. Lilach and A. Kolmakov, *Nano Lett.*, 2009, **9**, 2322-2326.

9. J. W. Byon, M.-B. Kim, M. H. Kim, S. Y. Kim, S. H. Lee, B. C. Lee and J. M. Baik, *J. Phys. Chem. C*, 2011, **116**, 226-230.
10. B. Hu, Y. Ding, W. Chen, D. Kulkarni, Y. Shen, V. V. Tsukruk and Z. L. Wang, *Adv. Mater.*, 2010, **22**, 5134-5139.
11. S.-H. Bae, S. Lee, H. Koo, L. Lin, B. H. Jo, C. Park and Z. L. Wang, *Adv. Mater.*, 2013, **25**, 5098-5103.
12. K. Liu, C. Cheng, Z. Cheng, K. Wang, R. Ramesh and J. Wu, *Nano Lett.*, 2012, **12**, 6302-6308.
13. I. S. Kim and L. J. Lauhon, *Crystal Growth & Design*, 2012, **12**, 1383-1387.
14. B. S. Guiton, Q. Gu, A. L. Prieto, M. S. Gudixsen and H. Park, *J. Am. Chem. Soc.*, 2005, **127**, 498-499.
15. J. I. Sohn, H. J. Joo, A. E. Porter, C.-J. Choi, K. Kim, D. J. Kang and M. E. Welland, *Nano Lett.*, 2007, **7**, 1570-1574.
16. J. M. Baik, M. H. Kim, C. Larson, A. M. Wodtke and M. Moskovits, *J. Phys. Chem. C*, 2008, **112**, 13328-13331.
17. L. Wei and M. L. Charles, *J. Phys. D: Appl. Phys.*, 2006, **39**, R387.
18. E. Strelcov, A. V. Davydov, U. Lanke, C. Watts and A. Kolmakov, *ACS Nano*, 2011, **5**, 3373-3384.
19. C. Cheng, K. Liu, B. Xiang, J. Suh and J. Wu, *Appl. Phys. Lett.*, 2012, **100**, 103111.
20. A. B. Djurisic, X. Chen, Y. H. Leung and A. Man Ching Ng, *J. Mater. Chem.*, 2012, **22**, 6526-6535.
21. P. Yang, H. Yan, S. Mao, R. Russo, J. Johnson, R. Saykally, N. Morris, J. Pham, R. He and H. J. Choi, *Adv. Funct. Mater.*, 2002, **12**, 323-331.
22. A. R. b. Mohd Yusoff, H. P. Kim and J. Jang, *Org. Electron.*, 2013, **14**, 858-861.
23. X. Y. Chen, F. Fang, A. M. C. Ng, A. B. Djurišić, W. K. Chan, H. F. Lui, P. W. K. Fong, C. Surya and K. W. Cheah, *Thin Solid Films*, 2011, **520**, 1125-1130.
24. A. M. C. Ng, X. Y. Chen, F. Fang, Y. F. Hsu, A. B. Djurišić, C. C. Ling, H. L. Tam, K. W. Cheah, P. W. K. Fong, H. F. Lui, C. Surya and W. K. Chan, *Appl. Phys. B*, 2010, **100**, 851-858.
25. Y. W. Zhu, H. Z. Zhang, X. C. Sun, S. Q. Feng, J. Xu, Q. Zhao, B. Xiang, R. M. Wang and D. P. Yu, *Appl. Phys. Lett.*, 2003, **83**, 144-146.
26. J. B. You, X. W. Zhang, P. F. Cai, J. J. Dong, Y. Gao, Z. G. Yin, N. F. Chen, R. Z. Wang and H. Yan, *Appl. Phys. Lett.*, 2009, **94**, 262105.
27. N. Liu, G. Fang, W. Zeng, H. Long, L. Yuan and X. Zhao, *Appl. Phys. Lett.*, 2009, **95**, 153505.
28. Z. Zhang, G. W. Meng, Q. L. Xu, Y. M. Hu, Q. Wu and Z. Hu, *J. Phys. Chem. C*, 2010, **114**, 189-193.
29. A. Sohn, H. Kim, D.-W. Kim, C. Ko, S. Ramanathan, J. Park, G. Seo, B.-J. Kim, J.-H. Shin and H.-T. Kim, *Appl. Phys. Lett.*, 2012, **101**, 191605.
30. H. Yin, M. Luo, K. Yu, Y. Gao, R. Huang, Z. Zhang, M. Zeng, C. Cao and Z. Zhu, *ACS Appl. Mater. Interfaces*, 2011, **3**, 2057-2062.
31. A. Srivastava, T. S. Herng, S. Saha, B. Nina, A. Annadi, N. Naomi, Z. Q. Liu, S. Dhar, Ariando, J. Ding and T. Venkatesan, *Appl. Phys. Lett.*, 2012, **100**, 241907.
32. Y. Li, S. Ji, Y. Gao, H. Luo and P. Jin, *ACS Appl. Mater. Interfaces*, 2013, **5**, 6603-6614.
33. J. A. Li and J. Dho, *J. Cryst. Growth*, 2010, **312**, 3287-3291.
34. Q.-A. Huang, M. Qin, B. Zhang and J. K. O. Sin, *J. Appl. Phys.*, 1997, **81**, 7589-7594.
35. J. Q. Xu, Y. M. Zhao, X. H. Ji, Q. Zhang and S. P. Lau, *J. Phys. D: Appl. Phys.*, 2009, **42**, 135403.
36. Q. Y. Zhang, J. Q. Xu, Y. M. Zhao, X. H. Ji and S. P. Lau, *Adv. Funct. Mater.*, 2009, **19**, 742-747.
37. C. X. Zhao, K. Huang, S. Z. Deng, N. S. Xu and J. Chen, *Appl. Surf. Sci.*, 2013, **270**, 82-89.
38. J. She, Z. Xiao, Y. Yang, S. Deng, J. Chen, G. Yang and N. Xu, *ACS Nano*, 2008, **2**, 2015-2022.